Supporting Information

Boron Vacancy: A strategy to boost the Oxygen Reduction Reaction of hexagonal boron nitride nanosheet in hBN-MoS₂ heterostructure

Dipayan Roy[†$], Karamjyoti Panigrahi[†$], Bikram K. Das[‡], Uday K. Ghorui[b], Souvik Bhattacharjee[‡], Madhupriya Samanta [†a], Sourav Sarkar[†], and Kalyan K. Chattopadhyay[†,‡]*

[†]School of Materials Science and Nanotechnology, Jadavpur University, Kolkata-700032, India

[‡]Department of Physics, Jadavpur University, Kolkata-700032, India

[a]Department of Electronics and Telecommunication Engineering, Jadavpur University, Kolkata 700032, India

[b]Indian Institute of Engineering Science and Technology, Shibpur. Howrah-711103

*Corresponding Author: kalyan_chattopadhyay@yahoo.com

S1. EXPERIMENTAL:

Reagents and chemicals

Hexagonal boron nitride (hBN) (1 μm grain size, 99% purity), Molybdenum (IV) sulphide (MoS₂), (<2 μm grain size, 98%), sodium cholate hydrate (99% purity), nafion (5 wt % solution H₂O), 20% Pt/C, potassium hydroxide (KOH, 99% purity), dimethyl-formamide (99% purity), from Merck were used for synthesis and application purposes. Deionized (DI) water was taken from a Direct-Q Millipore deionized (18 Ω at 25° C).

Synthesis of hBN Sheet

The hBN sheet utilized throughout this work was synthesized *via* a surfactant-based liquid exfoliation, sonication, and centrifugation methodology[1]. Liquid exfoliation was performed by adding bulk hBN powder into an aqueous solution of sodium cholate hydrate (concentration, 6 g/L) in a 100 mL beaker. The resultant dispersion was then sonicated using a probe sonicator (55% Power) for 1 hour, before a centrifugation step that was performed at 5000 rpm for 90 minutes. Following centrifugation, the corresponding supernatant was discarded and the resulting sediment was re-dispersed into Deionized water (2 g/L, 100 mL). Next, the solution was probe sonicated using a probe sonicator (PKS-750FM, max. power rating-15000 watt) for 5 hours. Upon completion of the sonication treatment, the solution was separated into 20 mL aliquots before each sample was centrifuged at 2000 rpm for 90 mins (separately). The sediment from this process contained un-exfoliated hBN that was consequently discarded. The remaining supernatant being subjected to a further centrifugation period at 5000 rpm for 90 minutes. Finally, the forthcoming supernatant was removed and found to contain the hBN sheet nanosheets that are utilized herein.

Preparation of hBN and MoS$_2$ heterostructure (HBPS) using Probe Sonicator

10 mg of hBN sheet and 10 mg of bulk MoS$_2$ powder was mixed with 40 ml of *N, N*-dimethyl formamide (DMF) and the mixture was stirred for 10 minutes at room temperature. The mixture was kept in probe sonicator and sonicated for 10 hours at a constant temperature of 30°C (55% Amplitude). The solution was then centrifuged at 1500 rpm for 30 min. The as-obtained residue at the bottom of the centrifuge was filtered under vacuum and dried at 60°C to obtain HBPS.

Preparation of (MS) using Probe Sonicator

The procedure to prepare MS is the same as HBPS without adding the hBN sheet.

S2. CHARACTERIZATION:

The diffraction patterns of all the synthesized powder samples were obtained from a Rigaku MiniFlex powder X-ray diffractometer over the scattering angle range $15° \leq 2\theta \leq 80°$ in steps of $0.02°$ using monochromatic CuK$_\alpha$ radiation at a measuring speed of $0.5°$ min^{-1}. The crystalline structures were refined by Rietveld's method using a pseudo-Voigt function to fit peak-profiles

employing the FULLPROF program[2]. Morphology was studied using a field emission scanning electron microscope (FESEM, Hitachi S-4800), high-resolution transmission electron microscope (JEOL 2100) operated at 200 kV. X-ray Photoelectron Spectroscopy (XPS) using a monochromatic Al K$_\alpha$ X-ray source (hυ =1486.6 eV) and a hemispherical analyser (SPECS HSA 3500), Fourier transformed infrared spectrophotometer (FTIR-8400S), Raman/AFM spectrometer (Witec Alpha300R, λex =532 nm) for structural and compositional analysis. Absorption maxima were determined by UV–Vis spectrophotometer (Shimadzu UV-3600). The Brunauer–Emmett–Teller (BET) surface area of the heterostructures was examined with a Quantachrome NovaWin2 Instrument at 77K.

XRD analysis

 The relationship between interplanar distance (d) and angle of reflection is (2θ) have explained from Bragg's equation as follows[3]:

$$d = \frac{\lambda}{2 * Sin\theta}$$

(1)

Where d is the interlayer spacing calculated in Å, λ is the incident wavelength of X-ray, θ is he half of the diffraction angle.

 Theoretical methods

All the first principles calculations were carried out using Vienna ab-initio simulation package (VASP)[4-5]. Generalized gradient approximation (GGA) along the projector augmented wave (PAW) approach was implemented during the geometry optimizations[6]. The exchange correlation terms of the energy Hamiltonian were dealt with the Perdew–Burke–Ernzerhof (PBE) functional as implemented in VASP[7]. Vacuum slab of length 24 Å was positioned in the direction normal to the 2D plane of the systems to ward off any spurious interaction. Γ centered (7×7×1) k-point mesh was used during the geometry optimization of the pristine systems whereas Γ centered (1×1×1) k-point mesh was used for the sufficiently large heterostructure. For density of states calculations, k point meshes of (30×30×1) and (7×7×1) were utilized for Brillouin zone integration of the pristine unit cells and the heterostructure system respectively. The effects of dispersive forces were taken into account via the DFT+D2 force field (Grimme's) method[8]. All the calculations were done in spin unrestricted manner. We have further investigated the origin of boron vacancy (B-vacancy) formation in the h-BN-MoS$_2$

3

heterostructure system by means of first principles calculations. The h-BN-MoS$_2$ heterostructure was made using a (5×5) and a (4×4) supercell of h-BN and MoS$_2$ unit cell respectively to minimize the strain on each layer. One boron atom was removed from the heterostructure and the defected system was allowed to relax completely. Each boron (B) and nitrogen (N) atom in the h-BN layer is equivalent. Hence, the mono-vacancy model was built by removing one B atom from the middle of the h-BN monolayer so that representation of the ORR mechanism remains uncomplicated and vacancies do not interact with their recurrent images. Distance between two formed B vacancies was found to be as large as 12.72 Å after geometry optimization and the interaction between two vacancies are expected to be reduced to its minimum. Within the MoS$_2$-hBN heterostructure, the h-BN supercell in its pristine form contains 25 boron atoms, one of which was removed during mono-vacancy formation resulting in B vacancy concentration of (1/25 x 100) % = 4%.

A mono-boron vacancy was similarly created in a free-standing h-BN monolayer of same dimension as in the heterostructure.

The neutral boron vacancy formation energies were calculated using the following equation:

$$E_f = E_v - E_p + n_B\mu_B \qquad\qquad (3)$$

Where E_f is the vacancy formation energy, E_v is the energy of the system with boron vacancy, E_p is the energy of the pristine system, n_B is the number of boron atom removed from the pure host and μ_B is the chemical potential of boron. μ_B was calculated from the rhombohedral α-boron system as reference. Lower formation energy as calculated using the equation (3) indicates better stability of the system after vacancy formation. Bader charge analysis was used to calculate the charge transfer between the atoms with and without the presence of boron vacancy[9]. The efficiency of the heterostructure was evaluated in terms of free energy and the free energy difference value for each ORR intermediate step was calculated using the following equation:

$$\Delta G = \Delta E + \Delta ZPE - T\Delta S, \qquad\qquad (4)$$

where, ΔE in the enthalpy of the reaction, ΔZPE is the zero point energy correction term which is ignored in our calculations due to its insignificant contribution the in the free energy in general and $T\Delta S$ is the entropy temperature term the value of which for gas phase molecules were taken from standard physical chemistry table[10]. The free energy of coupled proton and electron (H$^+$ + e$^-$) were calculated as suggested by Norskov et. al in their pioneering work[10].

The adsorption energies of di-oxygen molecule on the catalyst surface were calculated using the following formula

$$E_{ads} = E_{P+O2} - E_P - E_{O2} \tag{5}$$

Where E_{ads} is the di-oxygen molecule adsorption energy, E_{P+O2}, E_P and E_{O2} are the ground state energy of the O_2 adsorbed system, pristine catalyst, and free O_2 molecule respectively.

Electrochemical measurement

Electrochemical measurements were carried out in a typical three electrode system. A platinum (Pt) wire, Ag/AgCl (sat. 3.5 M KCl) electrode, and glassy carbon (GCE) were used as an auxiliary, a reference electrode, and a working electrode respectively. Finally, the potential was converted concerning the reversible hydrogen electrode (RHE) using

$$E_{RHE} = E_{Ag/AgCl} + (2.303RT/F)\ pH + E^{\circ}_{Ag/AgCl} \tag{6}$$

Where, $E^{\circ}_{Ag/AgCl}$ = 0.2 V at 30^0C, F is the Faraday constant (96 485 C mol^{-1}), R denotes Gas constants (8.314 J mol^{-1} K^{-1}), T is the temperature at which the experiment was carried out (30^0C). The pH was taken as 12 For 0.1 (M) KOH solution.

All electrochemical measurements were performed using an autolab PGSTAT (M204) potentiate/galvanostatic coupled to a computer using Nova 1.1 software.

The catalyst ink was prepared by dispersing the as synthesized materials (~1 mg) separately in DMF (1 ml) with 5% Nafion (100 μL) and then ultrasonicated for 10 min. The working electrode for each measurement was prepared by drop casting 3μL from stock solution on top of the working area of GCE and dried at 60°C in an oven after polishing the GCE with gamma alumina powder. All the measurements were performed in 0.1 M KOH as electrolyte saturated with O_2 gas (Indian Refrigeration system, India, 99.99% purity) in polytetrafluoroethylene (PTFE) container. Oxygen purging was done for 30 min before each measurement. The durability and methanol crossover test towards ORR were measured at a fixed potential -0.3 V vs. Ag/AgCl at 1600 rpm in 0.1 M KOH saturated with O_2. The cell was equipped with a 3 M saturated Ag/AgCl for reference electrode, Pt wire as a counter electrode and a glassy carbon electrode with a diameter of 3 mm as a working electrode. CV has measured before and after the long-time durability (3.5 hours) at a non-faradic region to calculate the double-layer capacitance (C_{dl}) and electrochemically active surface area (ESCA). For the crossover test, 2 (M) Methanol was added after 400 s for measurement of HBPS and 20% Pt/C. All the

measurements were performed at room temperature and current densities were calculated to the geometric area of the glassy carbon disk electrodes.

Electrochemical parameters

The diffusion of electrolytes elevates the current density by increasing the rotation rate which can be explained by Koutecky–Levich (K-L) approach[11].

Limiting and kinetic Current densities, electron transfer number have evaluated from K-L equation as follows:

$$\frac{1}{J} = \frac{1}{J_K} + \frac{1}{J_L} \qquad (7)$$

$$\frac{1}{J} = \frac{1}{J_K} + \frac{1}{B\omega^{1/2}} \qquad (8)$$

$$B = 0.21nFD^{2/3}C_0\upsilon^{-1/6} \qquad (9)$$

$$J_K = nFKC_0 \qquad (10)$$

where n is the number of electrons transferred in ORR, F is the Faraday constant (96 485 C mol^{-1}), v is the kinematic viscosity of the electrolyte (0.01 cm^2/ s), D is the diffusion coefficient of an oxygen molecule (1.9×10^{-5}cm^2/s), C_{O2} is the bulk concentration of oxygen (1.2×10^{-6}mol/cm^3)[19],ω is the rotation and J_k is the rate kinetic current density. Kinetic current density (J_k) and electron transfer rate constant (k) have calculated from the intercept K-L plot.

The percentage of peroxide generate within the intermediate and electron number are also calculated from RRDE tests following the Eqn [11].

$$H_2O_2\ (\%) = 200 * \frac{\dfrac{I_r}{N}}{\dfrac{I_r}{N} + I_d} \qquad (11)$$

$$n = 4 * \frac{I_d}{\dfrac{I_r}{N} + I_d} \qquad (12)$$

Where, I_d and Ir imply disk and ring current, current collection efficiency N=0.42.

Electrochemically active surface area (ESCA):

The ESCA is proportional to double-layer capacitance (C_{dl}) which is determined by CV at a non-Faradic region in 0.1 (M) KOH solution under different scan rates from 10 to 100 mV/s. The relationship between ESCA and C_{dl} is as follows[12-13]:

$$\text{ESCA} = \frac{Cdl}{Cs} \tag{13}$$

Where. Cs is the specific capacitance which is 40 $\mu F/cm^2$ per cm^2 for the flat electrode. The C_{dl} has calculated by plotting between ΔJ (mA/cm^2) ($J_{Anodic} - J_{Cathodic}$) vs. scan rate at a fixed potential 0.95 V vs. RHE.
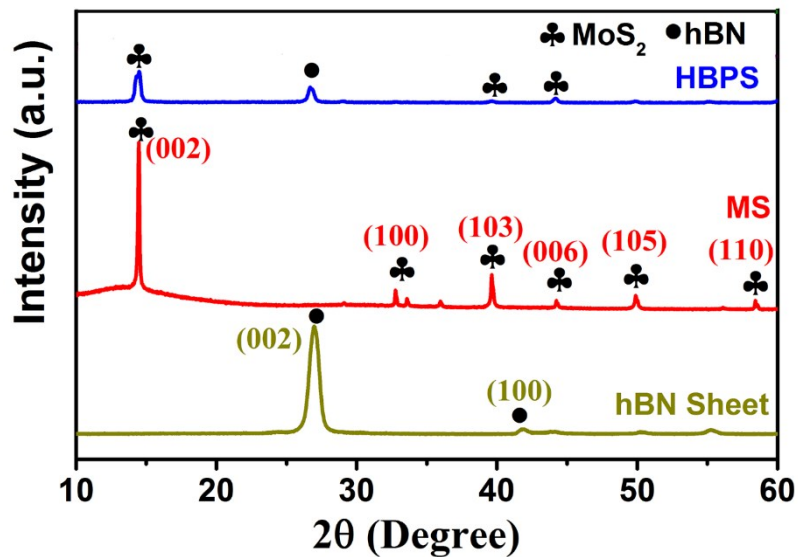
Figure S1: XRD patterns of hBN sheet, MS, and HBPS.
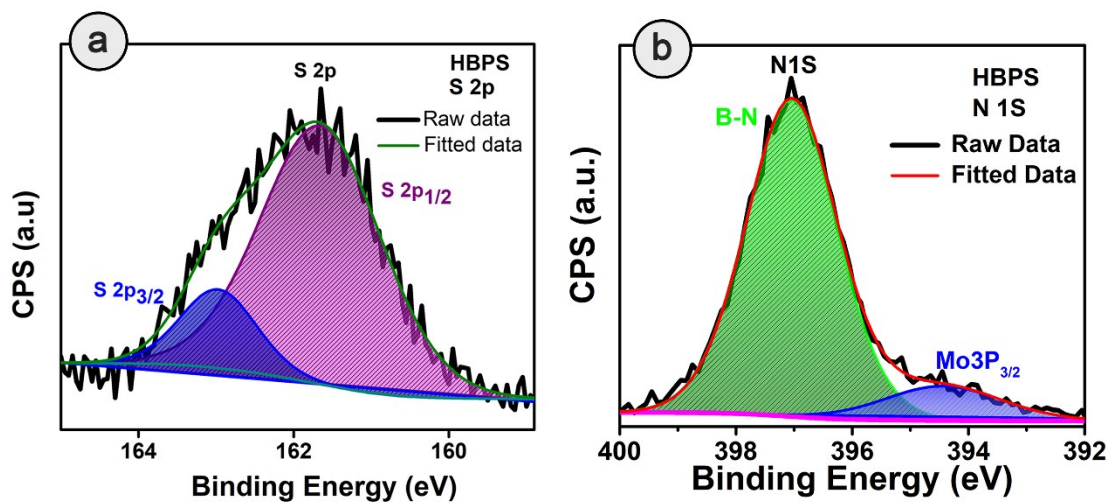
Figure S2: High resolution X-ray photoelectron spectroscopy (XPS) spectra of (a) S 2p (b) N 1s of HBPS.
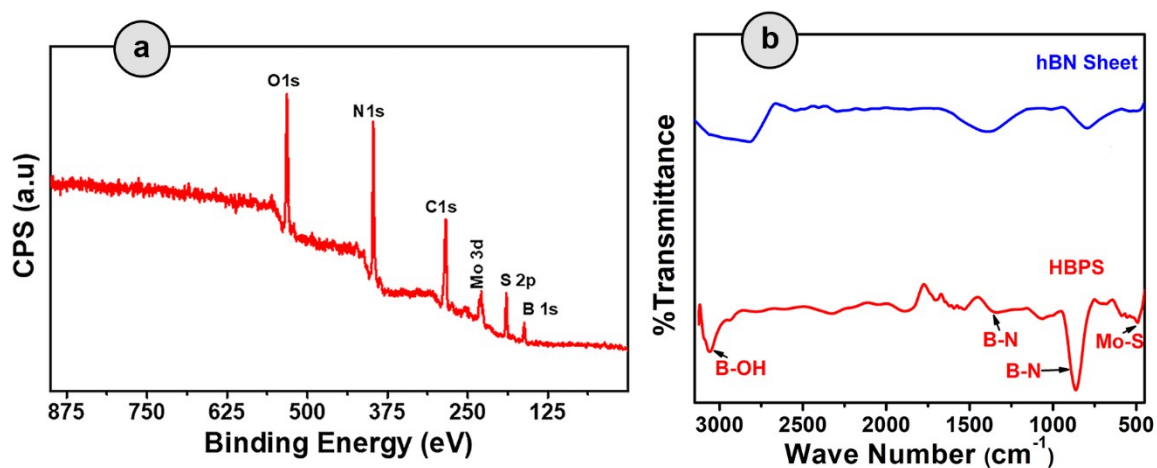
Figure S3: (a) X-ray photoelectron spectroscopy (XPS) survey of HBPS (b) FT-IR spectra of hBN sheet, and HBPS.
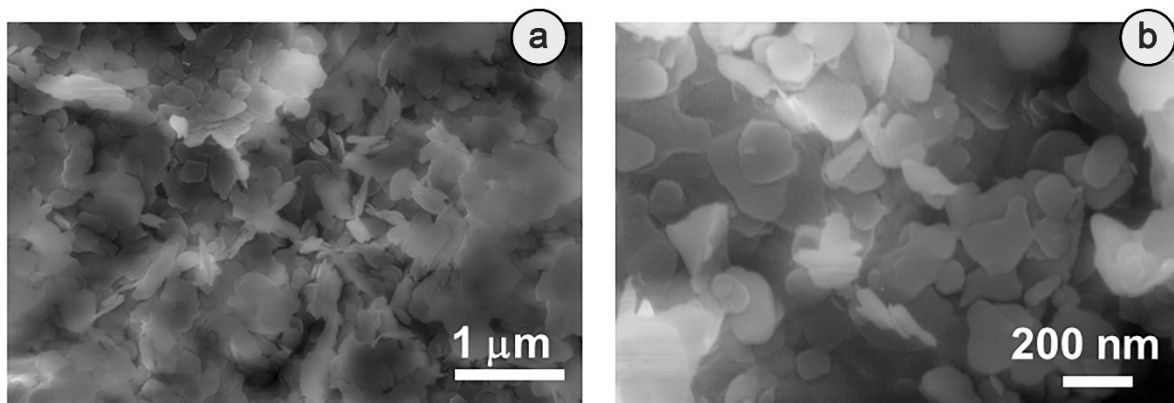
Figure S4: (a,b) FESEM Image of hBN sheet.
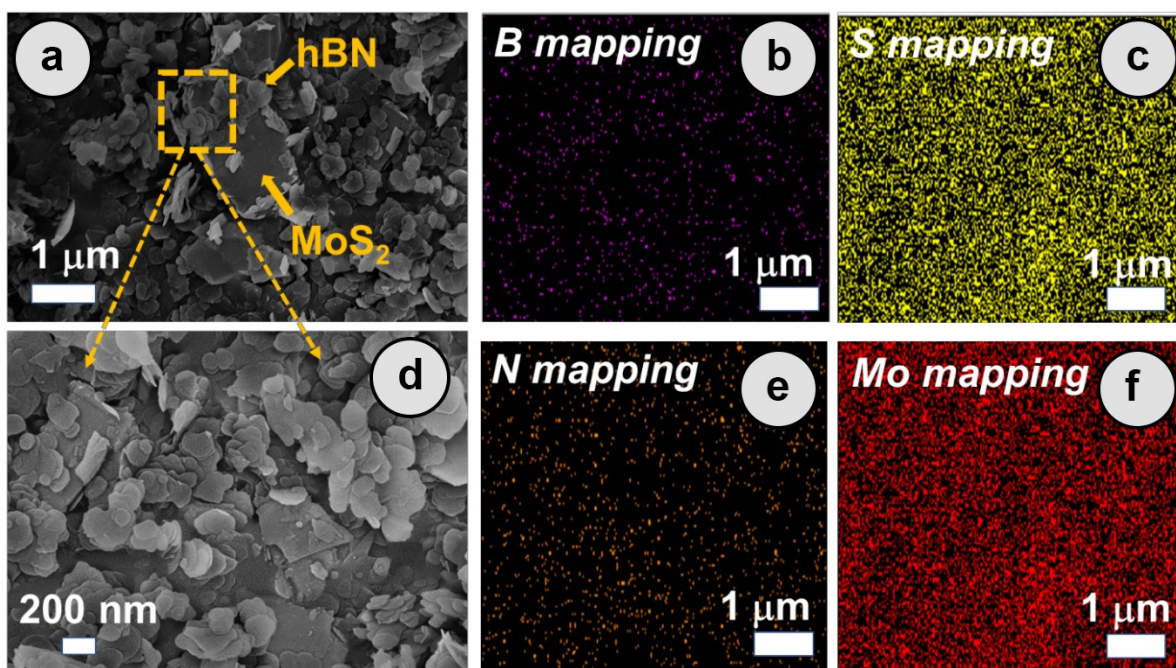
Figure S5: (a,b) FESEM Image of HBPS. (c-f) EDX mapping of HBPS containing Boron, sulfur, Nitrogen, and Mo.
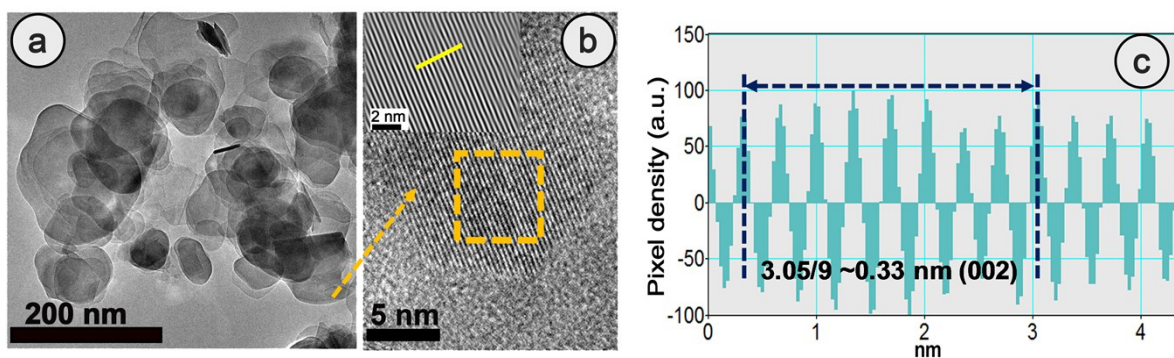
Figure S6: a) HRTEM image of hBN sheet (b) Fringe pattern of hBN sheet (c) Inverse fast Fourier transformation (IFFT) indicates (002) plane of hBN sheet.
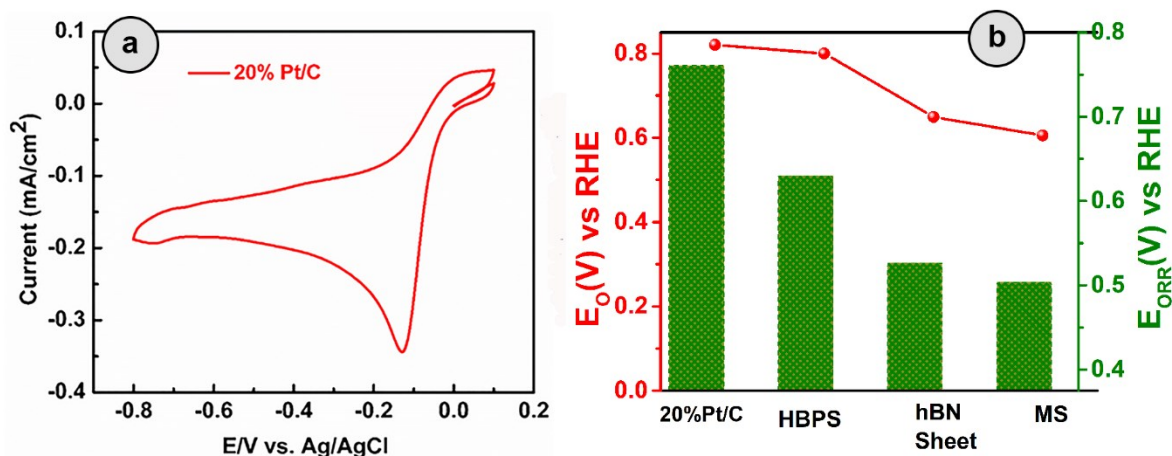
Figure S7: (a) Cyclic Voltammogram of (a) 20% Pt/C in O_2 saturated solution in 0.1 (M) KOH at 10 mV/s scan rate (b) Variation of E_{Onset} and E_{ORR} for 20% Pt/C, HBPS, MS, hBN sheet.
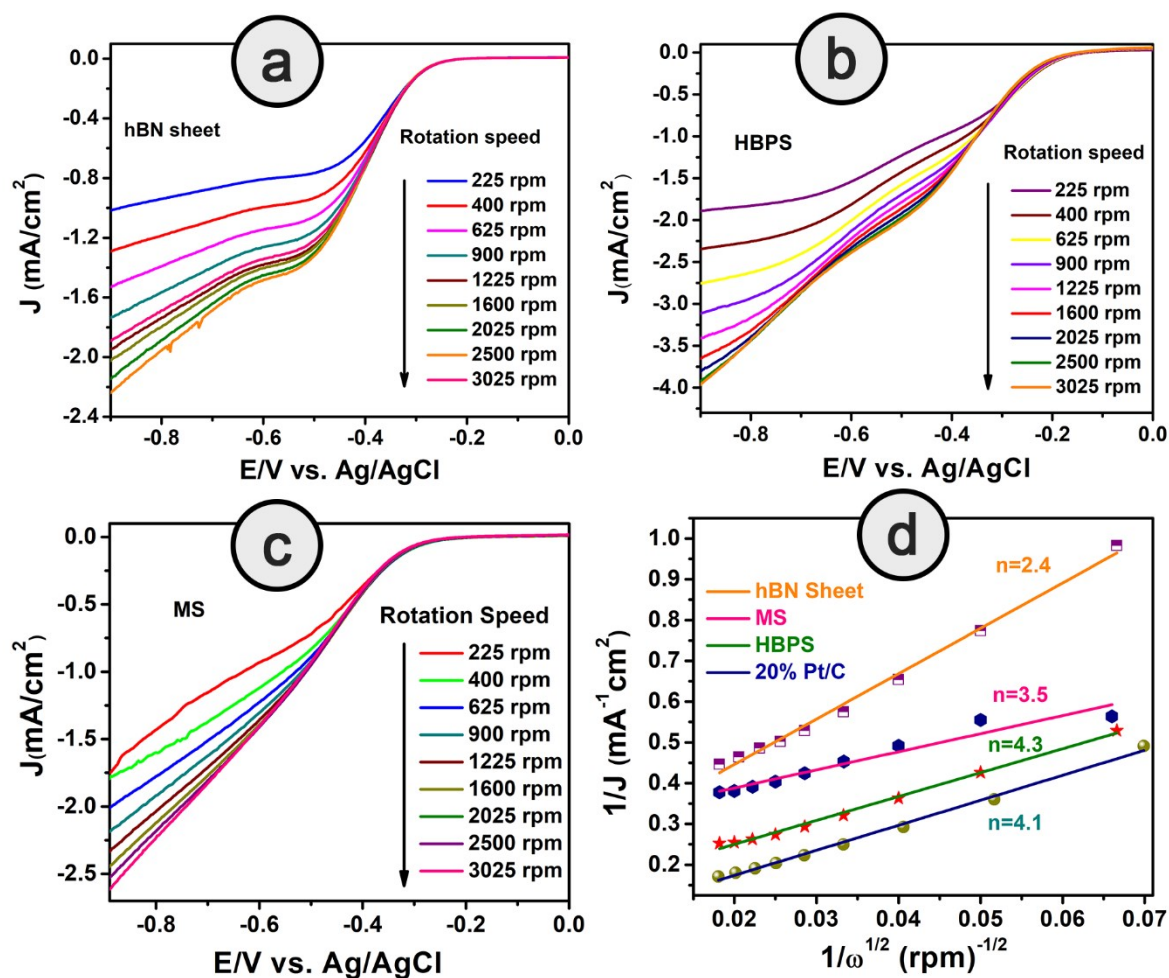
Figure S8: Linear sweep voltammogram of (a) hBN sheet (b) HBPS (c) MS in 0.1 (M) KOH at a scan rate 10 mV/s with different rotation speed (225-3025 rpm) via rotating disk electrode (RDE). (d) Koutecky-Levich (K-L) plot of 20 % Pt/C, hBN sheet, HBPS, MS at the different potential at -0.8 V vs. Ag/AgCl.
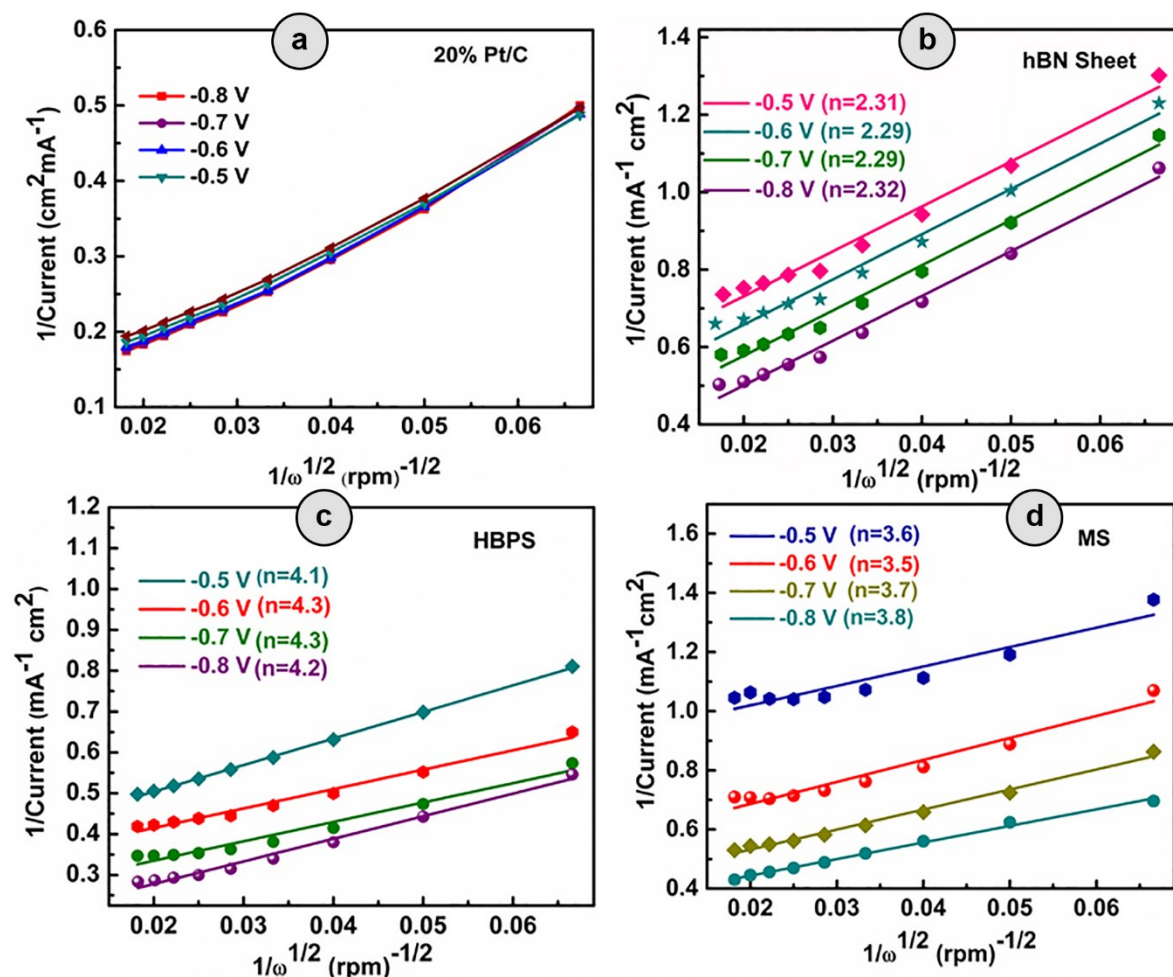
Figure S9: Koutecky-Levich (K-L) plot of (a) 20% Pt/C (b) hBN sheet (c) HBPS (d) MS at different potential from -0.8 V to -0.5 V vs. Ag/AgCl.
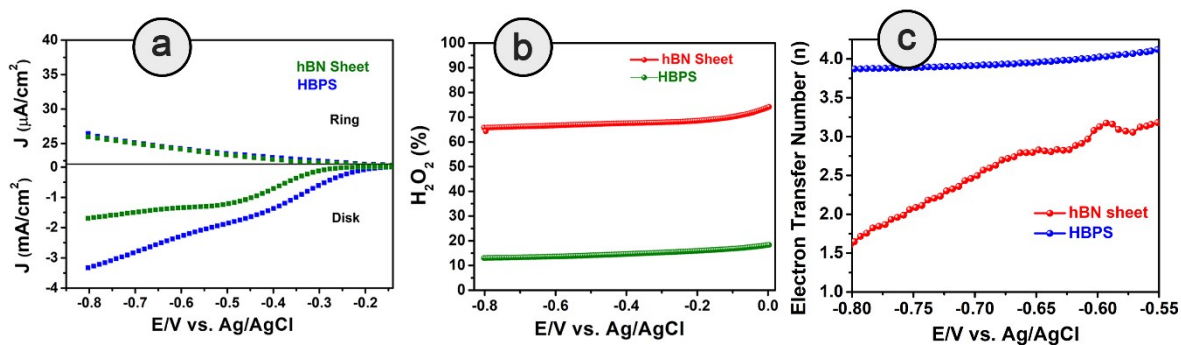
Figure S10: a) RRDE current-voltage curve at 25°C for 0.1 (M) KOH solution with GC electrode with rotation rate 1600 rpm. b) Percentage of H_2O_2 yield for various catalysts (C) Electron Transfer number of hBN sheet and HBPS from RRDE analysis.

.
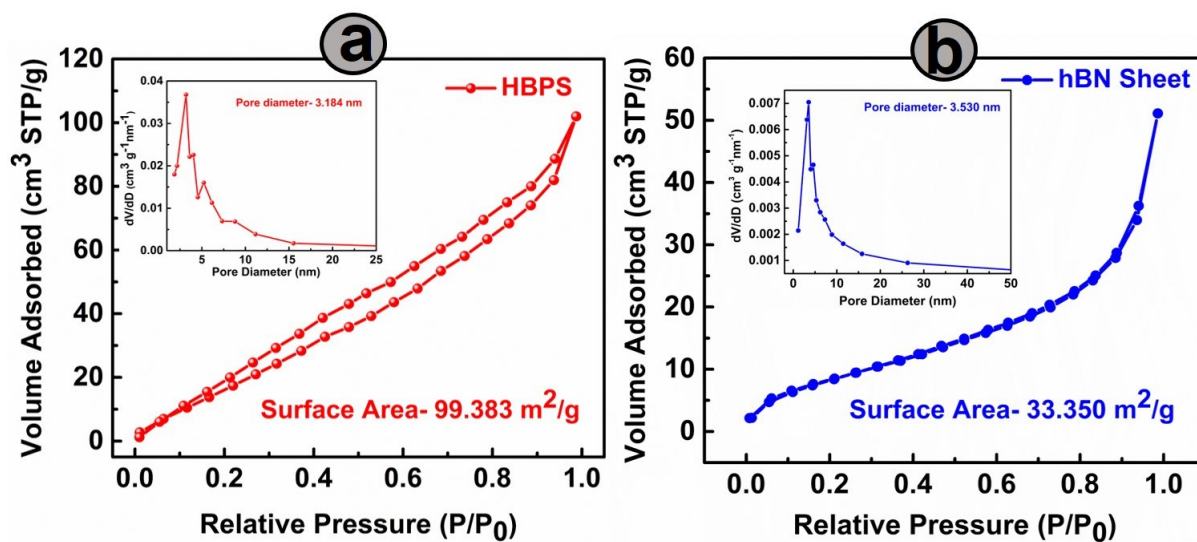
Figure S11: N_2 adsorption-desorption isotherm of (a) hBN sheet (b) HBPS. Inset showing the distribution of pore diameter with relative pressure.
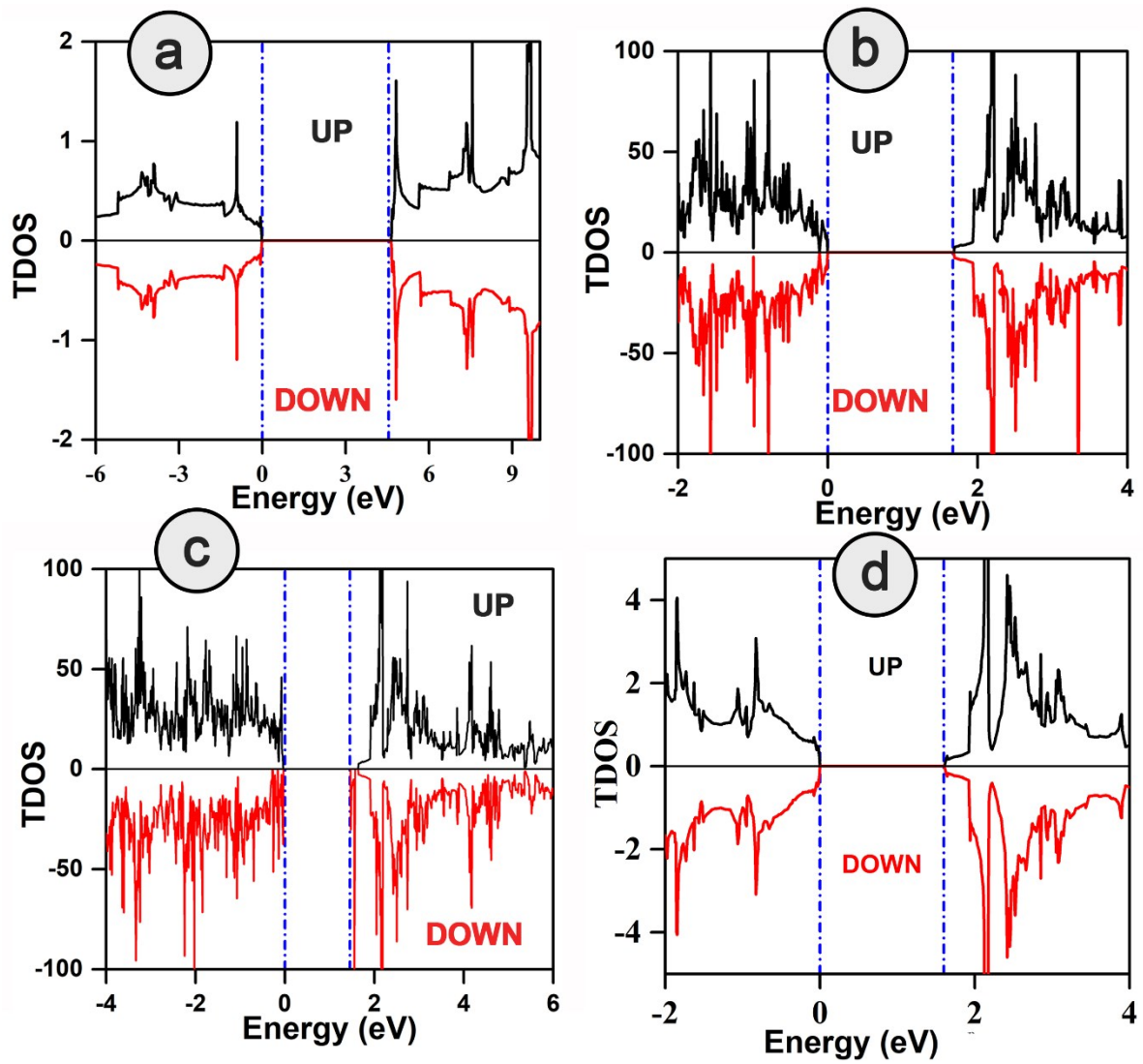
Figure S12: Band structure and DOS plot of (a) hBN, (b) hBN/MoS$_2$ heterostructure (c) B$_{vac}$-hBN-MoS$_2$ heterostructure and (d) MoS$_2$.
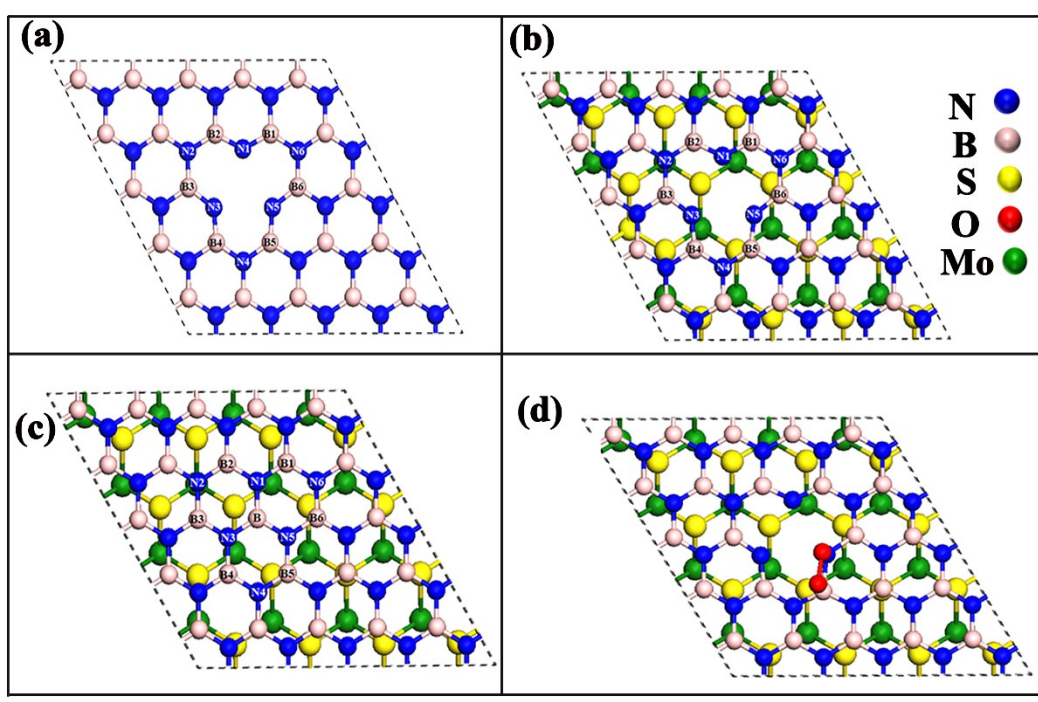
Figure S13: Top view of (a) hBN with boron vacancy (b) B_{vac}-hBN-MoS_2 (c) hBN-MoS_2 where the atom indexes correspond to the atoms for which amount of Bader charge transferred is shown in table S(5-7) (d) Top view of the adsorption of oxygen towards the active site of B_{vac}-hBN-MoS_2 during ORR.
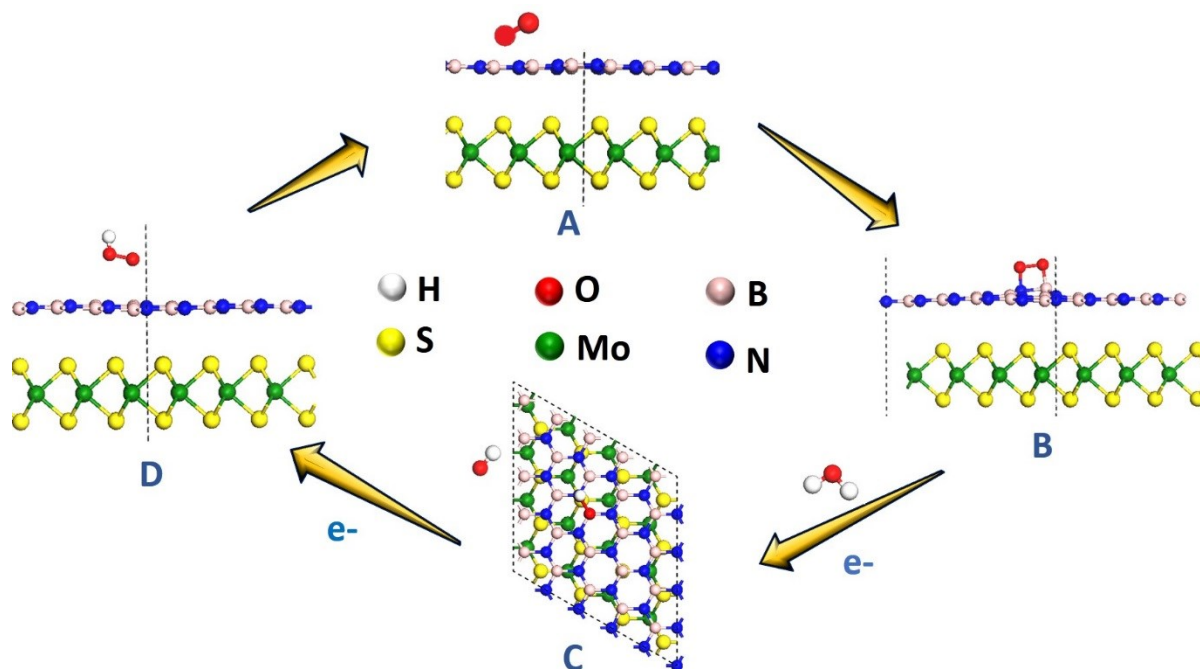
Figure S14: Two electron pathway ORR mechanism involving (A, B) adsorption of dioxygen molecule (O_2) on the B and N site; (C) peroxide (HO_2^-) ion formation on the active site and (D) after desorption of the peroxide ion of the hBN-MoS_2 heterostructure without boron vacancy.
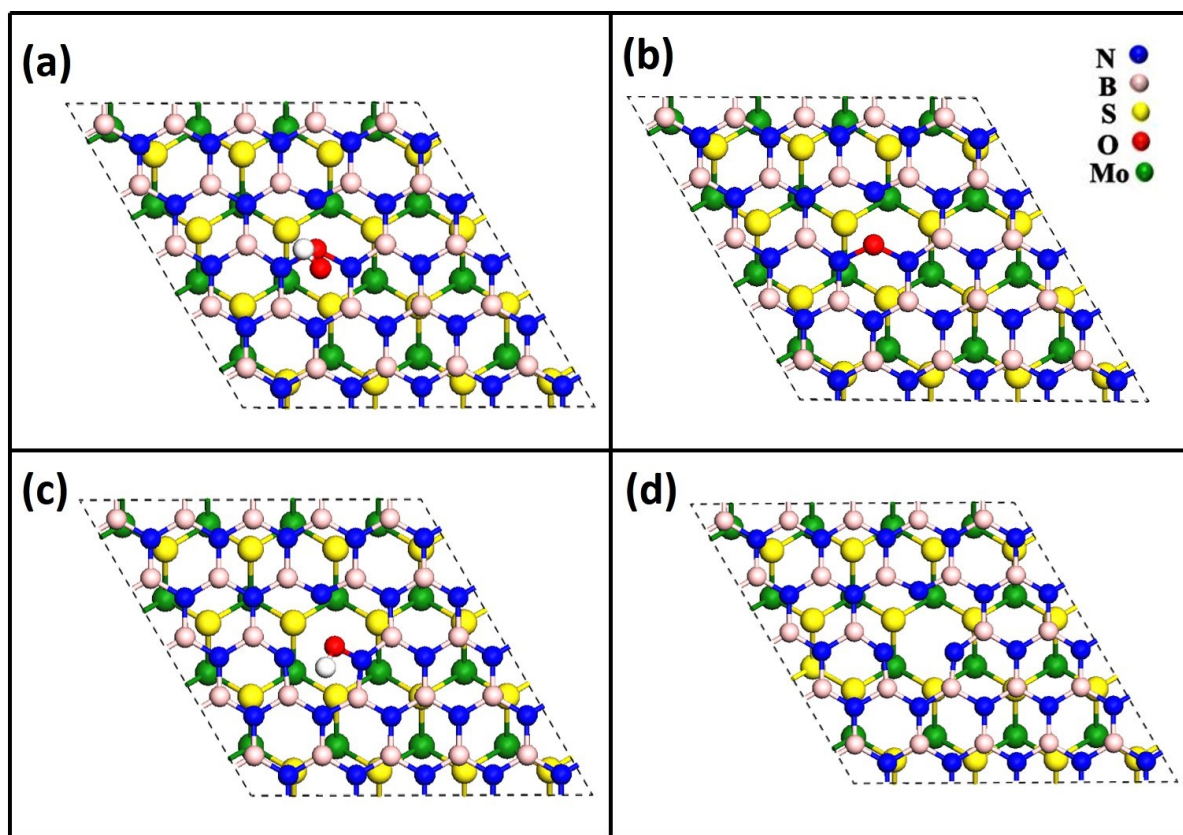
Figure S15: Top view of (a) *OOH formation (b) adsorbed oxygen (*O) into the vacancy site creates epoxy type bonding corresponds to Fig 4d (c) Hydroxyl ion formation on the active site corresponds to Fig 6e (d) after desorption of hydroxyl ion of the Bvac-hBN-MoS$_2$ heterostructure.
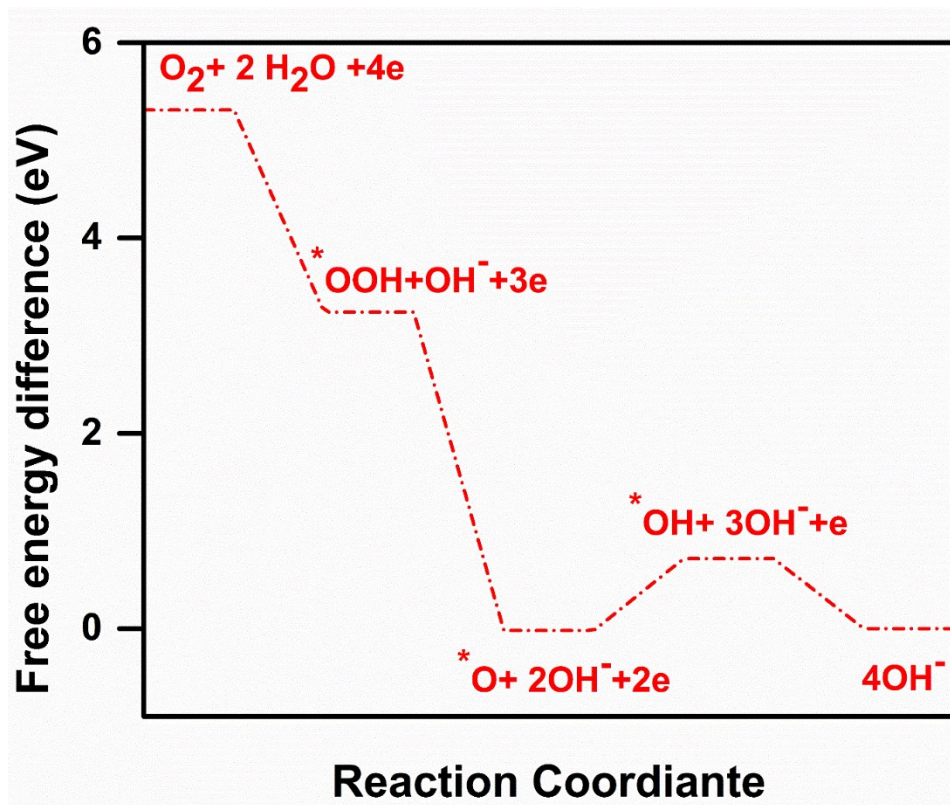
Figure S16: Gibbs Free energy (ΔG) diagram of ORR on B_{vac}-hBN-MoS$_2$ heterostructure system. Here * denotes surface adsorbed oxygen.
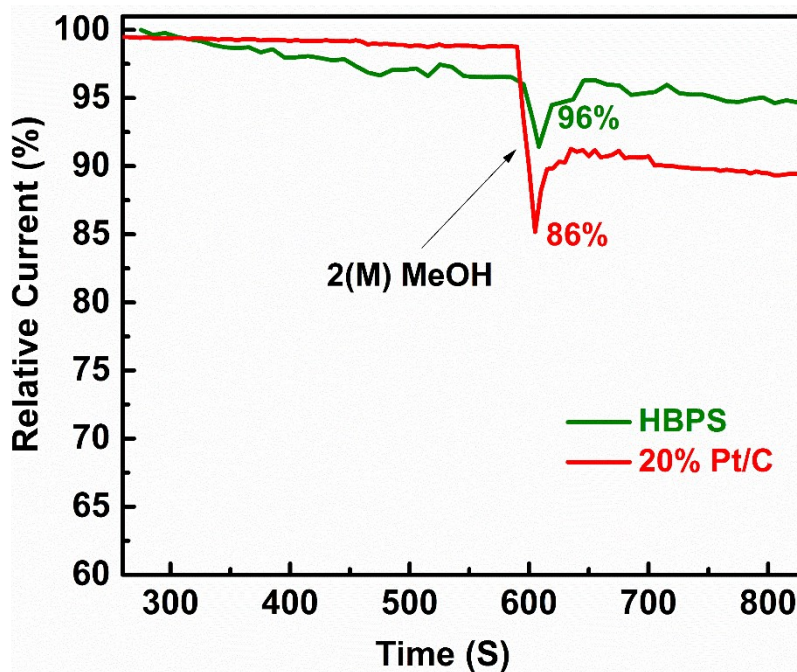
Figure S17: Tolerance of methanol of 20% Pt/C and HBPS at -0.3 V vs. Ag/AgCl in O$_2$ saturated 0.1 (M) KOH at 1600 rpm with the addition of methanol after 400 s.

Table S1. Refined crystallographic parameters obtained from XRD analysis.

Sample Name	Atom	x	y	z	Atomic Occupancy	Lattice parameters (Å)		Strain (η %)	Off-stoichiometry parameter (δ) for $hB_{(1-\delta)}N$	χ^2	Space-group
						$a=b$	c				
Bulk hBN	B	0	0	$1/2$	0.8337	2.506320	6.703041	0.0438	0.0570	1.36	P – 6m2 (No. 187) and Z = 2 $\alpha = 90°, \beta = 90°$ & $\gamma = 120°$
	B	$1/3$	$2/3$	0	0.92815						
	N	0	0	0	0.98791						
	N	$1/3$	$2/3$	$1/2$	1.00080						
hBN Sheet	B	0	0	$1/2$	0.75435	2.505496	6.703004	0.0487	0.0765	1.49	
	B	$1/3$	$2/3$	0	1.04117						
	N	0	0	0	0.93547						
	N	$1/3$	$2/3$	$1/2$	1.18449						
HBPS heterostructure	B	0	0	$1/2$	0.71388	2.505496	6.703001	0.0564	0.2884	1.67	
	B	$1/3$	$2/3$	0	0.52075						
	N	0	0	0	1.48826						
	N	$1/3$	$2/3$	$1/2$	1.42849						
	Mo	$1/3$	$2/3$	$1/4$	0.07653	3.168793	12.327536	0.0202			P 63/mmc
	S	$1/3$	$2/3$	0.623	0.14938						

Table S2: Different percentage of components deconvoluted from Mo 3d, S 2p, B 1s, and N 1s respectively of HBPS from XPS analysis.

Element Spectrum	Components	Position (eV)	Atomic %
Mo 3d	Mo 3d$_{5/2}$	231.7	52%
	Mo 3d$_{3/2}$	228.6	38%
	2S	225.3	18%
S 2p	S 2p$_{1/2}$	163	27.33%
	S 2p$_{3/2}$	161.7	72.67%
B 1s	B-N	189.8	98.85%

	B-O	192	1.15%
N 1s	B-N	397.1	95.69%
	Mo 3p$_{3/2}$	394.5	4.31%

Table S3: Different percentages of components of HBPS from XPS survey analysis.

Elements	Mo 3d	S 2p	B 1s	N 1s	O 1s	C 1s
% Components	4.38%	8.8%	17%	22.27%	12.65%	33.5%

Table S4: Comparison of the different parameters of ORR for all materials. All the potential has calculated in RHE.

Catalysts	E_{ORR} (V)	E_{Onset} (V)	J_L at 1600 rpm (mA/cm^2)	J_K at 0.1 (V) (mA/cm^2)	n	Tafel Slope (mV/Decade)
HBPS	0.63	0.80	3.6	5.96	~4.1	66
hBN Sheet	0.52	0.60	2	3.71	~2.5	72
MS	0.49	0.65	2	3.01	~3.3	74

Table S5: Comparison of C_{dl} and ESCA before the durability test.

Catalysts	C_{dl} (mF/cm^2)	ESCA (m^2/g)
HBPS	11.87	34.48
hBN Sheet	9.8	28.2
MS	3.1	9.3

Table S6: Charge transferred to/ from the atoms near the vacancy site for free standing hBN sheet with boron vacancy.

Atom index as denoted in figure S14	Charge transferred hBN with B-vacancy	Charge transferred (e) B_{vac}-hBN-MoS$_2$	Charge transferred hBN-MoS$_2$
N1	-1.569	-1.591	-2.141
N2	-2.147	-2.144	-2.159
N3	-1.564	-1.588	-2.148
N4	-2.161	-2.155	-2.153
N5	-1.579	-1.591	-2.151
N6	-2.161	-2.147	-2.156
B1	2.158	2.149	2.152
B2	2.155	2.154	2.146
B3	2.155	2.141	2.161
B4	2.158	2.150	2.155
B5	2.157	2.149	2.150
B6	2.157	2.148	2.143
B	-	-	2.154

Table S7: Comparison of ORR Performance of different 2D materials.

Catalyst	Electrode & Electrolyte	E_{ORR} (V)	E_{Onset} (V)	J_L at 1600 rpm	n	Ref.
2D-hBN/RGO	GC* & 0.1 M KCl	-	0.798 V vs. RHE	-3 mA/cm^2	3.7	14
Surfactant-exfoliated 2D hBN	SPE# & 0.1 (M) H$_2$SO$_4$	-0.71 V vs. SCE	-	-	-	15
Nitrogen-doped MoS$_2$/carbon	GC & 0.1 M KCl	-	-	-2.78 mA/cm^2	-	16
2D-MoS$_2$	SPE & 0.1 (M) H$_2$SO$_4$	-0.53 V vs. SCE	0.16 V vs. SCE	-	4	17
Nb doped MoS$_2$	GC & 0.1 (M) KOH	0.61 V vs. RHE	0.78 V vs. RHE	-	-	18
AuNP/MoS$_2$	GC & 0.1 (M) KOH	-0.41 V vs. SCE	-0.12 V vs. SCE	-3 mA/cm^2	-	19
MoS$_2$-rGO Nanosheets	GC & 0.1 (M) KOH	-	0.8 V vs. RHE	-2.72 mA/cm^2	3.3	20
Co(OH)$_2$ -MoS$_2$ /rGO	GC & 0.1 (M) KOH	0.7 V vs. RHE	0.805 V vs. RHE	-4.1 mA/cm^2	3.2-3.6	21
2D-hBN	SPE & 0.1 (M) H$_2$SO$_4$	-0.81 V vs. SCE	-	-	2.45	22
MoS$_2$ Quantum Dots	GC & 0.1 M NaOH	-0.5 V vs. Ag/AgCl	0.27 V vs. RHE	-1.4 mA/cm^2	1.8	23
CoOx/mC@MoS$_2$	GC & 0.1 (M) KOH	-	0.67 V vs. RHE	-2.4 mA/cm^2	2.68-3.2	24
PdxSy-MoS$_2$ /N-GR	RDE$ & 0.1 (M) KOH	-	-0.242 V vs. SCE	-4.2 mA/cm^2	3.75-3.8	25
Porus BCN catalyst	GC & 0.1 (M) KOH	0.8 V vs. RHE	0.94 V vs. RHE	-5 mA/cm^2	3.93	26
O-MoS$_2$-87	GC & 0.1 (M) KOH	-	0.94 V vs. RHE	-3.1 mA/cm^2	4	27
Nanostructured MoS$_2$	GC & 0.1 (M) KOH	-	-0.14 V vs. Ag/AgCl	-2.4 mA/cm^2	-	28
hBN/MoS$_2$ (HBPS)	(GC) & 0.1 (M) KOH	-0.28 V vs. Ag/AgCl (0.63 V vs. RHE)	0.80 V vs. RHE	~3.70 mA/cm^2	~4.1	This Work

*GC: Glassy Carbon; #SPE: screen-printed graphite electrode; $RDE: Ring disk electrode.

REFERENCES

1. R. J Smith, P. J King, M. Lotya, C. Wirtz, U. Khan, S. De, A. O'Neill, G.S. Duesberg, J.C. Grunlan, G. Moriarty, J. Chen, J. Wang, A. I Minett, V. Nicolosi, J.N. Coleman, *Adv. Mater.,* 2011, **23 (34)**, 3944–3948.

2. J. Rodríguez-Carvajal, *Phys. B Condens. Matter*, 1993, **192 (1–2)** ,55–69.

3. P. Saini, R. Sharma, N. Chadha, *Indian Journal of Pure & Applied Physics (IJPAP),* 2017, **55(9)**, 625-629.

4.   G. Kresse, J. Hafner, . *Phys. Rev. B,* 1993, **47 (1)**, 558–561.

5. G. Kresse, J. Hafner, *Phys. Rev. B,* 1994, **49 (20)**, 14251–14269.

6 P. E Blöchl,. *Phys. Rev. B,* 1994, **50 (24)**, 17953–17979.

7 J. P Perdew, K. Burke, M. Ernzerhof, *Phys. Rev. Lett.,* 1996, **77 (18)**, 3865–3868.

8 S. Grimme, *J. Comput. Chem.,* 2006, **27 (15)**, 1787–1799.

9. W. Tang, E. Sanville, G.A. Henkelman, *Condensed Matter.,* 2009, **21(8)**, 084204.

10. S. Back, S. Siahrostami, *Nanoscale Adv.* 2019, **1 (1)**, 132–139.

11. R. Zhou, Y. Zheng, M. Jaroniec, S.Z. Qiao, *ACS Catal.,* 2016, **6 (7)**, 4720–4728.

12. X. Li, Y. Fang, X. Lin, M. Tian, X. An, Y. Fu, R. Li, J. Jin, J. Ma, *J. Mater. Chem. A.,* 2015, **3 (33)**, 17392–17402.

13. H. Deng, C. Zhang, Y. Xie, T. Tumlin, L. Giri, S. P Karna, J. Lin, *J. Mater. Chem. A.,* 2016, **4 (18)**, 6824–6830.

14. I. M Patil, M. Lokanathan, B. Kakade, *J. Mater. Chem. A.,* 2016. **4 (12)**, 4506–4515.

15. A. F Khan, M. P Down, G. C Smith, C. W Foster, C. E Banks, *J. Mater. Chem. A.,* 2017, **5 (8)**, 4103–4113.

16. L . Hao, J. Yu, X. Xu, L. Yang, Z. Xing, Y. Dai, Y. Sun, J. Zou,. *J. Power Sources.,* 2017, **339**, 68–79.

17. S. J Rowley-Neale, G. C Smith, C. E Banks, *ACS Appl. Mater. Interfaces.,* 2017, **9 (27)**, 22539–22548.

18. X. J Chua, J. Luxa, A. Y. S Eng, S. M Tan, Z. Sofer, M. Pumera, *ACS Catal.,* 2016, **6 (9)**, 5724–5734.

19. T. Wang, J. Zhuo, Y. Chen, K. Du, P. Papakonstantinou, Z. Zhu, Y. Shao, M.Li, *ChemCatChem.,* 2014, **6 (7)**, 1877–1881.

20. J. Zhou, H. Xiao, B. Zhou, F. Huang, S. Zhou, W. Xiao, D. Wang, *Appl. Surf. Sci.,* 2015,

358, 152–158.

21.   R . Illathvalappil, S. M Unni, S. Kurungot,. *Nanoscale.*,2015, **7 (40)**, 16729–16736.

22.   A. F Khan, E. P Randviir, D. A. C Brownson, X. Ji, G. C Smith, C. E Banks, *Electroanalysis*, **29 (2)** (2017) 622–634.

23.   K.K Tadi, A.M Palve, S. Pal, P.M Sudeep, T.N Narayanan,.*Nanotechnology*.,2016, **27(27)**,275402.

24.   L. He, B. Cui, J. Liu, M. Wang, Z. Zhang, H. Zhang, *ACS Sustain. Chem. Eng.*,2018, **6 (7)**, 9257–9268.

25.   L. G Bach, M. L. N Thi, Q.B. Bui, H. T Nhac-Vu, *Synth. Met.*,2019, **254**,172–179.

26.   J. Wang, J. Hao, D. Liu, S. Qin, D. Portehault, Y. Li, Y. Chen, W. Lei, *ACS Energy Letters*.,2017, **2(2)**,306–312.

27.   H. Huang, X. Feng, C. Du, S. Wu, W. Song, *J. Mater. Chem. A.,*2015, **3 (31)**, 16050–16056.

28.   C.Suresh, S.Mutyala, J. Mathiyarasu, *Mater. Lett.*, 2016, **164**, 417–420.